

Changes to ENSO under CO₂ Doubling in a Multimodel Ensemble

WILLIAM J. MERRYFIELD

Canadian Centre for Climate Modelling and Analysis, Meteorological Service of Canada, Victoria, British Columbia, Canada

(Manuscript received 6 June 2005, in final form 2 December 2005)

ABSTRACT

An EOF analysis is used to intercompare the response of ENSO-like variability to CO₂ doubling in results from 15 coupled climate models assembled for the Intergovernmental Panel on Climate Change Fourth Assessment Report. Under preindustrial conditions, 12 of the 15 models exhibit ENSO amplitudes comparable to or exceeding that observed in the second half of the twentieth century. Under CO₂ doubling, three of the models exhibit statistically significant ($p < 0.1$) increases in ENSO amplitude, and five exhibit significant decreases. The overall amplitude changes are not strongly related to the magnitude or pattern of surface warming. It is, however, found that ENSO amplitude decreases (increases) in models having a narrow (wide) ENSO zonal wind stress response and ENSO amplitude comparable to or greater than observed. The models exhibit a mean fractional decrease in ENSO period of about 5%. Although many factors can influence the ENSO period, it is suggested that this may be related to a comparable increase in equatorial wave speed through an associated speedup of delayed-oscillator feedback. Changes in leading EOF, characterized in many of the models by a relative increase in the amplitude of SST variations in the central Pacific, are in most cases consistent with effects of anomalous zonal and vertical advection resulting from warming-induced changes in SST.

1. Introduction

Because it is the leading mode of climate variability on interannual time scales and impacts weather patterns across much of the globe, El Niño–Southern Oscillation (ENSO) has direct and substantial impacts on society. The intensity and frequency of El Niño and La Niña events are known to have varied in recent decades (e.g., Wang and An 2001), as well as in the more distant past (e.g., Tudhope et al. 2001). These changes appear to be connected to shifts in climate, raising the possibility that ENSO might undergo discernible changes in response to anthropogenically driven warming.

All investigations of this issue face an inherent challenge in identifying secular changes to ENSO in the presence of multidecadal modulations unrelated to climate change (e.g., Knutson et al. 1997), and most to date have focused on one or at most two coupled models. An early study by Meehl et al. (1993) found, based on short 15-yr time series, that while CO₂ doubling led

to little change in ENSO amplitude or period, there was a distinct eastward shift in the pattern of equatorial SST variability. Tett (1995) examined ENSO differences between a 75-yr control run and one in which CO₂ increased at a rate of 1% yr⁻¹, and also found no obvious changes in the amplitude of equatorial SST variability. Much longer 1000-yr simulations in which CO₂ was held at present-day values or increased at 1% yr⁻¹ until stabilization at 2 × CO₂ or 4 × CO₂ were considered by Knutson and Manabe (1994) and Knutson et al. (1997). They found >20% decreases in equatorial SST variability in both the 2 × CO₂ and 4 × CO₂ experiments, which exceeded centennial-scale variability in the control run. There were no obvious changes in period, although the center of SST variability did shift eastward as in Meehl et al. (1993).

Each of the above studies employed ocean models having a coarse resolution of between 2.5° and 5° in latitude/longitude and exhibited ENSO-like SST variability in the present epoch somewhat weaker than is observed. A model having a much higher ocean meridional resolution of 0.5° in the Tropics was discussed by Timmermann et al. (1999), who compared ENSO variability in a 300-yr control run with one forced to year 2100 by increasing greenhouse gases according to the

Corresponding author address: Dr. William Merryfield, Canadian Centre for Climate Modelling and Analysis, University of Victoria, P.O. Box 1700, Victoria BC V8W 2Y2, Canada.
E-mail: bill.merryfield@ec.gc.ca

Intergovernmental Panel on Climate Change (IPCC) IS92a scenario. In this model the amplitude of ENSO-related SST variability was found to be realistic in the control run (although its period was too short), and increased dramatically near the end of the greenhouse warming run. This increase was ascribed to a warming-induced strengthening of the tropical thermocline, leading to increased eastern Pacific SST response to a given wind stress anomaly. The increase was greater than any such change in the control run, although the consideration of only a single realization and the difficulty inherent in separating warming-related trends from decadal and longer time-scale variability as discussed by Knutson et al. (1997) make such attribution less than certain. Collins (2000a) also inferred warming-induced increases in ENSO amplitude, as well as decreases in period, in various elevated-CO₂ integrations of the second Hadley Centre Coupled Ocean–Atmosphere General Circulation Model (HadCM2), especially a 4 × CO₂ run. The amplitude increase was ascribed to a steepened temperature gradient in the thermocline resulting from warmer surface temperatures as in Timmermann et al. (1999), and the period decrease to an increased meridional temperature gradient near the equator, leading to more rapid changes in thermocline heat content and hence a shorter ENSO cycle according to the recharge oscillator picture of Jin (1997). Such changes were less pronounced or absent at 2 × CO₂, and in 4 × CO₂ runs of the HadCM3 model (Collins 2000b), although they could be induced by imposing a substantial artificial heat flux at the equator. The ENSO changes in HadCM2 thus appeared to be associated with the equatorial warming and increased mean meridional temperature gradients near the equator, which were more pronounced than in HadCM3. More recently, Zelle et al. (2005) found little change in ENSO amplitude, frequency, or pattern under climate warming in version 1.4 of the Community Climate System Model (CCSM1.4), which simulates ENSO fairly realistically in the present epoch. A detailed analysis led them to conclude that this lack of sensitivity is unrealistic and is due to the wind stress response to equatorial SST anomalies being too meridionally confined; this, they argued, leads to an ENSO oscillation that is unrealistically stable, and hence insensitive to climate change, and to a short ENSO period because of the equatorial confinement, and hence more rapid propagation speeds of equatorial waves as discussed by Kirtman (1997).

Because these and other coupled models differ in many respects in their representation of ENSO-like variability, conclusions drawn by examining the behavior of one or two models may not be robust. It is therefore desirable to extend such studies to encompass a

larger sample of models. An ideal opportunity for such investigations has arisen from the recent assemblage of climate model output in support of the IPCC Fourth Assessment Report (AR4). Using results from 23 coupled models including those considered by AR4, Guilyardi (2006) examined relationships between ENSO and the mean climate and seasonal cycle in the tropical Pacific, as well as changes in ENSO properties under CO₂ doubling and quadrupling from preindustrial control conditions in instances where such scenarios were available. He concluded that, although both increases and decreases in ENSO amplitude were found under elevated CO₂, models that exhibited the most realistic mixtures of SST–wind feedbacks (i.e., local SST–wind interactions versus remote thermocline wind interactions) tended to show significant increases in ENSO amplitude. Van Oldenborgh et al. (2005) examined, in 17 models, differences between ENSO in twentieth century (or in one case preindustrial) climate simulations and in 50 yr of elevated CO₂ simulations under the Special Report on Emissions Scenarios (SRES) A2 scenario, SRES A1B scenario, or 1% yr⁻¹ to CO₂ doubling scenarios. Although both increases and decreases in ENSO amplitude were found among the models, they concluded that because these changes did not exceed observed decadal variations in ENSO, they could not be considered significant. Meehl et al. (2006) found decreases in ENSO amplitude under a variety of CO₂ increase scenarios in the National Centers for Atmospheric Research (NCAR) Parallel Climate Model (PCM) and version 3 of the Community Climate System Model (CCSM3) models, which they ascribed, at least partially, to a weakening of the equatorial thermocline due to reduced wind-driven meridional overturning in the upper ocean.

The present paper seeks to quantify, relatively precisely, any warming-induced changes to ENSO in this current generation of coupled climate models. Fifteen models were considered to meet selection criteria, outlined in section 2, that enable the statistical significance of the changes to be assessed. In all, approximately 8000 yr of monthly averaged model output have been analyzed. To mitigate complications of assessing ENSO statistics in a nonstationary climate, differences in ENSO between a preindustrial control climate and a warmer climate in which CO₂ concentrations have stabilized at twice their preindustrial value are considered. To assess the likelihood that the changes found are attributable to increased CO₂ concentrations rather than sampling variability, control run output is divided into 100-yr segments to create samples of centennial time series whose inherent variability can be compared with apparent warming-related changes.

Section 2 describes this methodology and the associated EOF analysis. In sections 3, 4, and 5 changes in modeled ENSO amplitude, period, and spatial pattern are examined, and possible reasons for the changes are discussed. Conclusions are presented in section 6.

2. Methodology

a. Model selection

In a study such as this it is desirable that sufficient model output be available to enable the statistical significance of any warming-related changes to ENSO to be assessed, since, as pointed out by Knutson and Manabe (1994, 1998) and Knutson et al. (1997), such changes can potentially be confused with decadal-to-century-scale modulations of ENSO that occur in the absence of forced climate change. It is helpful in addition to minimize complications associated with assessing statistical properties of ENSO in a nonstationary climate. Based on these two factors, the comparison considered here is between ENSO in a low-CO₂ climate in which greenhouse gas concentrations are fixed at preindustrial (1860) levels with a CO₂ concentration of 288 ppm, and a high-CO₂ climate in which CO₂ has increased from 1860 levels at a rate of 1% yr⁻¹ for 70 yr, until CO₂ concentration has doubled, and is held fixed thereafter. (This is the “1pcto2x” scenario.) In the low-CO₂ preindustrial control runs, model climates are expected to remain relatively stable for centuries, with changes limited to any drifts intrinsic to the models. In the high-CO₂ case, climate is obviously highly nonstationary during the period of CO₂ increase, but after CO₂ concentrations stabilize the rate of climate change should decrease, with lesser changes continuing to occur because of the relatively long response time scale of the oceans to increases in atmospheric CO₂ (e.g., Knutson et al. 1997). Although IPCC guidelines request that the simulations continue for 150 yr after CO₂ doubling is attained, at time of this study the entire 150 yr was not available for all models. Therefore, to maximize data availability while minimizing climate drift, the first 100 yr of simulation following stabilization at doubled CO₂ is taken to represent a high-CO₂ climate. Typically only one such interval was available for a given model, although for two of the models multiple realizations were obtained.

ENSO statistics derived from the 100-yr monthly time series for 2 × CO₂ climate are compared with those obtained from multiple 100-yr records from the preindustrial simulations. (In all such time series linear trends and the mean seasonal cycle are removed.) This eliminates the influence of any variability occurring on time scales of 100 yr or longer in the control climate. In

addition, because several such records typically are available for multicentury preindustrial control runs, by analyzing each 100-yr interval separately a sample is obtained that enables the significance of ENSO differences between the 2 × CO₂ and control climates to be assessed in terms of the century-to-century differences within the control run.

Of the models having output submitted to the IPCC data center at PCMDI, 15 satisfied or nearly satisfied the criteria that at least three centuries of preindustrial control and one full century of simulation following CO₂ stabilization were available. These models are listed in Table 1, along with their near-equatorial atmospheric and ocean resolutions and the numbers of available 100-yr preindustrial and 2 × CO₂ time series, denoted by N_{PICTL} and $N_{2\times\text{CO}_2}$. Several models were included despite not strictly meeting the selection criteria. These included the Goddard Institute for Space Studies (GISS) ER and the Institute of Atmospheric Physics (IAP) FGOALS-g1.0 models, for which the last 20 yr of 1% yr⁻¹ CO₂ increase and the first 80 yr of CO₂ stabilization were used to represent the 2 × CO₂ climate; the NCAR PCM1 model, for which the last 4 yr of CO₂ increase and the first 96 yr of stabilization were used; and the Met Office (MO) HadCM3 model, for which the first century following stabilization at 550 ppm CO₂ (about 1.9 times preindustrial concentration) in the SRES B1 scenario was used to represent high-CO₂ climate.

b. EOF analysis

Although ENSO variability is often characterized in terms of indices of SST variability in particular regions in the equatorial Pacific, patterns of SST variability differ from model to model. Hence it is desirable to characterize ENSO variability in terms of a model’s “own” ENSO through an EOF analysis. ENSO variability is considered to be represented by leading EOF1 of anomalous monthly SST in a region 10°S–10°N, 120°E–90°W that nearly spans the equatorial Pacific, and by time series of the corresponding first principal component (PC1).

Details of the analysis are as follows. Because of the greater availability of atmospheric model output at the time of this study, the SST was obtained from the atmospheric surface skin temperature. Grid cells having land fractions >1% (principally near New Guinea) were excluded from the analysis.¹ Information was re-

¹ Although grid resolution is generally finer in the ocean model than in the atmospheric model, consideration of SST variations on the atmospheric grid can be justified by noting that these are what determine the atmospheric model response.

TABLE 1. Description of models considered. Ensemble sizes N_{PICTL} and $N_{2\times\text{CO}_2}$ represent the numbers of available centuries of preindustrial control climate and of first centuries of stabilization at $2 \times \text{CO}_2$ ($N_{2\times\text{CO}_2} > 1$ if there are multiple realizations of the 1% per year to CO_2 doubling scenario). INM denotes the Institute of Numerical Mathematics; other group acronyms are defined in text.

| Group/model | Atmospheric resolution | Equatorial ocean resolution | N_{PICTL} | $N_{2\times\text{CO}_2}$ |
|-----------------------|-----------------------------------|-------------------------------------|--------------------|--------------------------|
| CCCMA/CGCM3.1(T63) | T63L31 | $1.4^\circ \times 0.9^\circ$ L29 | 3 | 1 |
| CCSR/MIROC3.2(medres) | T42L20 | $1.4^\circ \times 0.5^\circ$ L43 | 5 | 1 |
| CNRM/CM3 | T63L45 | $2^\circ \times 0.5^\circ$ L31 | 4 | 1 |
| GFDL/CM2.0 | $2.5^\circ \times 2^\circ$ L24 | $1^\circ \times 1/3^\circ$ L50 | 5 | 1 |
| GFDL/CM2.1 | $2.5^\circ \times 2^\circ$ L24 | $1^\circ \times 1/3^\circ$ L50 | 5 | 1 |
| GISS/EH | $5^\circ \times 4^\circ$ L20 | $2^\circ \times 2^\circ$ L16 | 4 | 1 |
| GISS/ER | $5^\circ \times 4^\circ$ L20 | $5^\circ \times 4^\circ$ L13 | 5 | 1 |
| IAP/FGOALS-g1.0 | T42L26 | $1^\circ \times 1^\circ$ L33 | 3 | 3 |
| INM/CM3.0 | $5^\circ \times 4^\circ$ L21 | $2.5^\circ \times 2^\circ$ L33 | 3 | 1 |
| IPSL/CM4 | $2.5^\circ \times 3.75^\circ$ L19 | $2^\circ \times 1^\circ$ L31 | 3 | 1 |
| MPI/ECHAM5 | T63L31 | $1.5^\circ \times 1.5^\circ$ L40 | 5 | 3 |
| MRI/CGCM2.3.2 | T42L30 | $2.5^\circ \times 0.5^\circ$ L23 | 3 | 1 |
| NCAR/CCSM3.0 | T85L26 | $1.125^\circ \times 0.27^\circ$ L27 | 7 | 1 |
| NCAR/PCM1 | T42L26 | $0.94^\circ \times 0.5^\circ$ L32 | 3 | 1 |
| MO/HadCM3 | $3.75^\circ \times 2.5^\circ$ L19 | $1.25^\circ \times 1.25^\circ$ L20 | 3 | 1 |

tained on the native model grids; that is, no interpolation to a common grid was performed. In constructing the covariance matrix, cells lying only partially in the region of interest were weighted by the square roots of the included areas.

EOFs are normalized to have unit spatial variance, and hence the variances of each PC reflect spatiotemporal variances of corresponding SST anomalies, and the variances of all the PCs sum to total SST variance in the study region. Power spectra of PC1 time series were computed by applying split-cosine tapering to the first and last 10% of each time series and were smoothed using a 24-bin Parzen window, which is free of sidelobes and associated variance leakage exhibited by some other spectral estimators (e.g., von Storch and Zwiers 1999).

3. ENSO amplitude

a. Amplitude changes in the multimodel ensemble

Changes in ENSO amplitude under CO_2 doubling are apparent in Fig. 1, which illustrates for each model PC1, PC2,² and total SST variances for the preindustrial climate (blue labels) and the $2 \times \text{CO}_2$ climate (red labels). Error bars indicate bias-corrected estimates of standard deviation, that is,

$$\left[\sum_{i=1}^N (x_i - \bar{x})/(N - 1) \right]^{1/2},$$

where x_i are the sampled values, N is the sample size, and \bar{x} is the sample mean, where each sample is obtained from $N > 1$ centennial time series. The observed variances, computed from 40 yr (1955–94) of version 2 of the Global Sea Ice and Sea Surface Temperature (GISST2) dataset, are indicated at far left.

One result that is immediately apparent is that PC1 variance is comparable to or greater than the observed variance in 12 of the 15 models. Also evident is the lack of any obvious systematic trend with respect to changes in SST variance under CO_2 doubling. In some of the models, PC1 and total SST variance increase rather dramatically [e.g., Max Planck Institute for Meteorology (MPI), Meteorological Research Institute (MRI)], even in relation to the standard deviations of the control samples. In others, a pronounced decrease is evident [e.g., IAP, Institut Pierre-Simon Laplace (IPSL)]. The magnitudes of sampling variations in these quantities also varies widely, being relatively largest in the Geophysical Fluid Dynamics Laboratory (GFDL) Coupled Climate Model, version 2.1 (CM2.1), GISS EH, MPI, and MO HadCM3, and smallest in Centre National de Recherches Météorologiques (CNRM) and IAP, both of which have large amplitudes and (as will be seen later) narrowband spectra. Corresponding measures of ENSO amplitude consisting of preindustrial rms PC1 (units: $^\circ\text{C}$) and its percentage change under CO_2 doubling are summarized in Table 2, along with the percentage contributions of PC1 and PC2 to total SST variance.

² PC2 is related to ENSO nonlinearity, specifically the asymmetry of SST response to upward versus downward thermocline displacements in the eastern Pacific (e.g., Monahan 2001; Monahan and Dai 2004), where EOF2 is concentrated in observations and in nearly all the models.

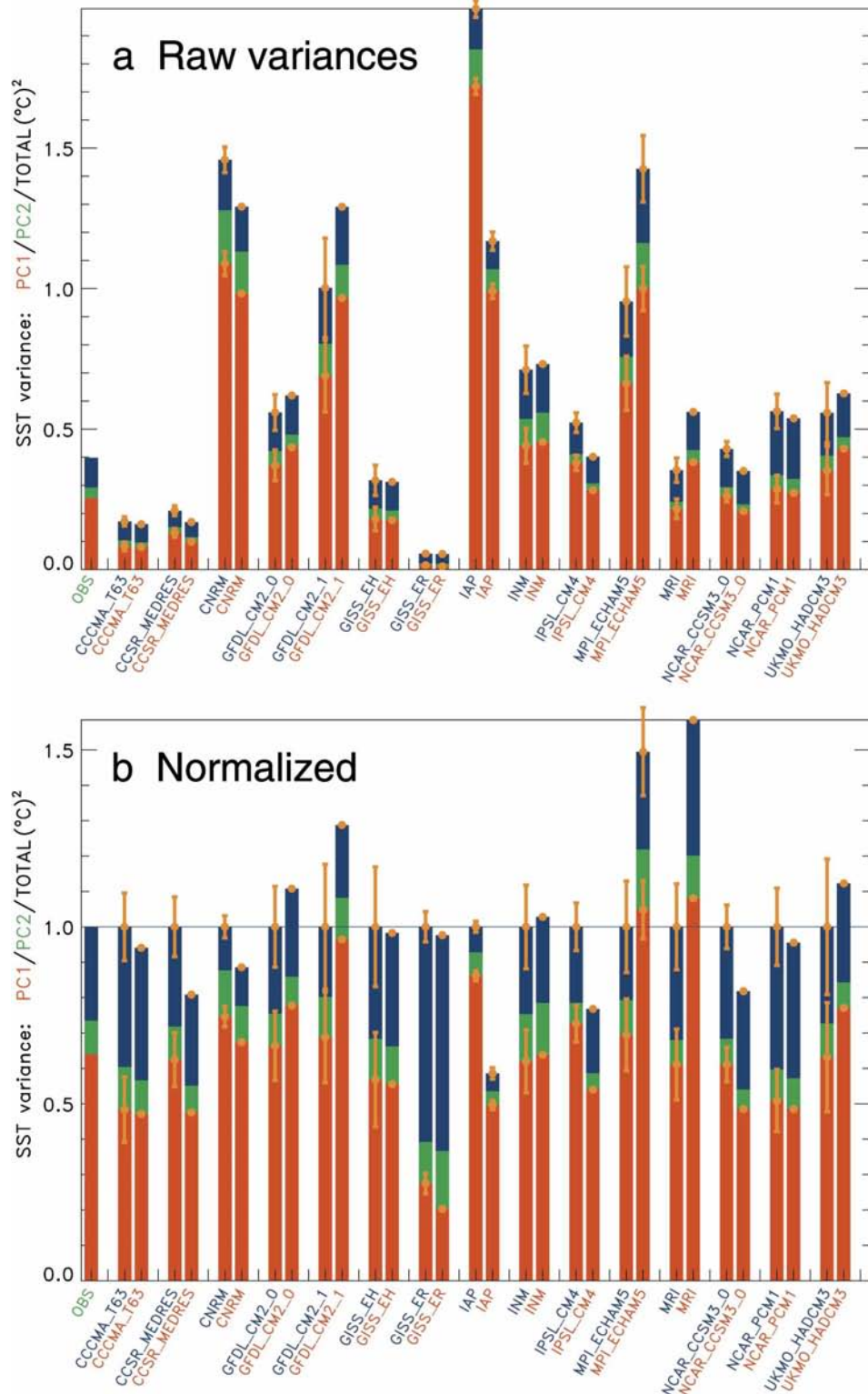


FIG. 1. (a) PC1 (red), PC2 (green), and total variances (blue) of monthly near-equatorial Pacific SST under preindustrial conditions (blue labels) and stabilized $2 \times \text{CO}_2$ conditions (red labels) for each of the 15 models considered. Observed variances based on monthly GISST SST data for 1955–94 are indicated at the far left. The error bars represent standard deviations σ obtained from samples of centennial time series in cases where three or more centuries of model output are available. (b) Same as in (a) but the variances are normalized according to $(\text{total preindustrial SST variance}) = 1$.

TABLE 2. Quantities relating to ENSO amplitude and its change under CO₂ doubling.

| Group/model | Rms PC1 (°C) | PC1 % of tot variance | PC2 % of tot variance | Δrms PC1 (%) | p value* |
|-----------------------|-----------------|--------------------------|--------------------------|-----------------|----------|
| CCCMA/CGCM3.1(T63) | 0.29 ± 0.03 | 48.0 ± 4.8 | 12.1 ± 1.2 | -0.9 | >0.2 |
| CCSR/MIROC3.2(medres) | 0.36 ± 0.02 | 62.3 ± 2.2 | 9.4 ± 0.7 | -12.6 | 0.12 |
| CNRM/CM3 | 1.04 ± 0.02 | 74.6 ± 0.6 | 13.1 ± 0.4 | -5.0 | 0.09 |
| GFDL/CM2.0 | 0.61 ± 0.05 | 66.2 ± 2.5 | 9.1 ± 0.7 | 8.5 | >0.2 |
| GFDL/CM2.1 | 0.83 ± 0.08 | 68.7 ± 2.1 | 11.3 ± 1.9 | 18.9 | 0.10 |
| GISS/EH | 0.42 ± 0.05 | 56.3 ± 3.8 | 11.5 ± 0.9 | -0.6 | >0.2 |
| GISS/ER | 0.12 ± 0.01 | 27.4 ± 1.8 | 11.7 ± 0.6 | -14.0 | 0.07 |
| IAP/FGOALS-g1.0 | 1.31 ± 0.01 | 86.2 ± 0.1 | 6.6 ± 0.1 | -24.1 | <0.01 |
| INM/CM3.0 | 0.66 ± 0.05 | 61.9 ± 1.7 | 13.3 ± 0.5 | 1.7 | >0.2 |
| IPSL/CM4 | 0.62 ± 0.02 | 72.6 ± 0.6 | 5.8 ± 0.2 | -13.8 | 0.07 |
| MPI/ECHAM5 | 0.81 ± 0.06 | 69.4 ± 1.8 | 9.8 ± 1.4 | 23.0 | <0.01 |
| MRI/CGCM2.3.2 | 0.46 ± 0.04 | 60.9 ± 2.6 | 6.9 ± 0.4 | 33.3 | 0.04 |
| NCAR/CCSM3.0 | 0.51 ± 0.02 | 61.1 ± 1.2 | 7.3 ± 0.3 | -10.8 | 0.04 |
| NCAR/PCM1 | 0.53 ± 0.05 | 50.7 ± 3.5 | 8.8 ± 0.5 | -2.1 | >0.2 |
| MO/HadCM3 | 0.59 ± 0.07 | 62.8 ± 3.1 | 9.4 ± 0.4 | 11.0 | >0.2 |
| GISST2 1955–94 | 0.50 | 64 | 9 | — | — |

* Probability according to a two-sided *t* test that differences between 2 × CO₂ and preindustrial PC1 variances equaling or exceeding those in Fig. 1 occur through random sampling from a normal distribution.

To illustrate how these apparent changes relate to variability within the control sample, histograms of the changes in total and PC1 variance in units of estimated standard deviations σ from the respective control samples are plotted in Fig. 2. (In instances where there are $N_{2 \times \text{CO}_2} > 1$ realizations of 2 × CO₂ stabilization, each realization is weighted by $N_{2 \times \text{CO}_2}^{-1}$ so that each model contributes equal area to the histogram.) As a null hypothesis we suppose that the differences in Fig. 1 have arisen through sampling of random intercentennial variations in total and PC1 variance that are normally distributed. If this were the case and if σ for each model were known accurately, then the histograms would tend toward similarly normalized 1 σ -wide Gaussians (thin curves in Fig. 2). However, because the standard deviations are not known exactly but are estimated from small samples of size N_{PICTL} , the distributions corresponding to the null hypothesis are better represented by *t* distributions for $N_{\text{PICTL}} - 1$ degree of freedom, which have broader tails; for example, the thick curves in Fig. 2 represent the extreme $N_{\text{PICTL}} = 3$ case.

The statistical significance of the differences can further be quantified through a two-tailed *t* test applied to each model. The resulting *p* values, summarized in the last column of Table 2, are the probabilities that differences as large or larger than those realized would arise under the null hypothesis. This probability is >0.2 for only 6 of the 15 models. If we take $p \leq 0.1$ as indicating statistical significance, then it is seen that three of the models (GFDL CM2.1, MPI, and MRI) exhibit signifi-

cant increases in PC1 variance under CO₂ doubling, whereas five (CNRM, GISS ER, IAP, IPSL, and NCAR CCSM3) exhibit significant decreases. If $p \leq 0.05$ is instead taken as a threshold, then MPI and MRI exhibit significant increases, and IAP and NCAR CCSM3 exhibit significant decreases.

b. Influence of SST changes

One influence cited as possibly governing ENSO amplitude changes is a change in the strength of the tropical thermocline (e.g., Timmermann et al. 1999; Collins 2000a,b), as discussed in section 1. As a measure of such changes, the mean SST warming $\Delta \bar{T}_{\text{mean}}$ under CO₂ doubling in the control region 10°S–10°N, 120°E–90°W (see Table 3 and the first column of Fig. 3) is considered.³ Because subsurface warming generally lags surface warming, the latter provides some indication of changes in thermocline strength, as illustrated for example in Fig. 1 of Timmermann et al. (1999) and Fig. 15 of Collins (2000a), although changes in ocean circulation can exert a contrary influence (Meehl et al. 2006). The change in ENSO amplitude associated with CO₂ doubling, described as the fractional change in rms PC1 (cf. Table 2), is plotted as a function of $\Delta \bar{T}_{\text{mean}}$ in Fig. 4a. No strong relation between ENSO amplitude change and $\Delta \bar{T}_{\text{mean}}$ is evident; in fact if one model

³ Incomplete availability of model output at the time of this study precluded the direct determination of thermocline intensity from subsurface ocean temperatures.

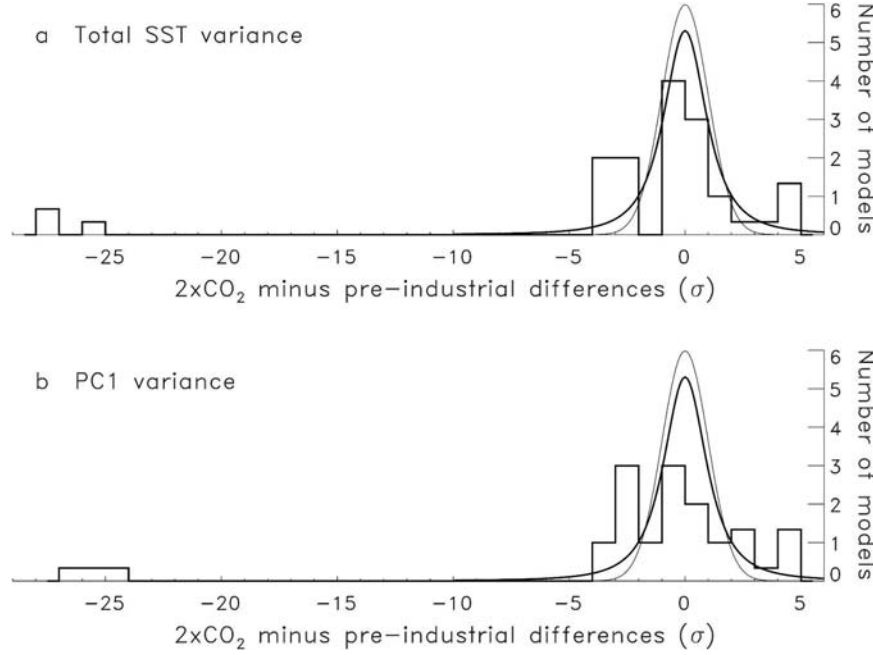


FIG. 2. Histograms of $2 \times \text{CO}_2$ minus preindustrial differences in (a) total SST variance and (b) PC1 variance for the 15 models in units of standard deviations σ estimated from the samples of centennial preindustrial time series. (In instances where multiple realizations of $2 \times \text{CO}_2$ stabilization output are available, i.e., $N_{2 \times \text{CO}_2} > 1$, each realization is assigned a weight $1/N_{2 \times \text{CO}_2}$) If the centennially sampled preindustrial variances were distributed normally and ENSO did not change under CO_2 doubling, the histograms would tend toward normal distributions (thin curves) if the σ were known exactly, and toward two-degree-of-freedom t -distributions (thick curves) if all the σ were estimated from $N_{\text{PC1TL}} = 3$ samples.

(MRI) having particularly large \bar{T}_{mean} is excluded, the correlation coefficient becomes small and negative. Thus, thermocline intensification does not appear to strongly govern changes in ENSO amplitude in the

multimodel ensemble, provided \bar{T}_{mean} serves as a reasonable proxy for increased subsurface vertical temperature gradients as assumed. This result is also evident from the fact that, although all models exhibit

TABLE 3. Quantities relating to $\Delta\bar{T}(x, y)$, the difference in temporal-mean SST between $2 \times \text{CO}_2$ and preindustrial climates in the control region 10°S – 10°N , 120°E – 90°W ; $\text{corr}(\Delta T, \text{EOF1})$ is the correlation of $\Delta\bar{T}$ with leading EOF1 of tropical Pacific SST, $\Delta\bar{T}_{\text{eq}} - \Delta\bar{T}_{10}$ is the difference between $\Delta\bar{T}$ zonally averaged at the equator and at $\pm 10^\circ$ latitude, and $(\Delta\bar{T}_{\text{eq}} - \Delta\bar{T}_{10})/\Delta\bar{T}_{\text{mean}}$ is this difference expressed as a fraction of $\Delta\bar{T}_{\text{mean}}$, the mean warming in the study region.

| Group/model | $\text{Corr}(\Delta T, \text{EOF1})$ | $\Delta\bar{T}_{\text{eq}} - \Delta\bar{T}_{10}$ (°C) | $(\Delta\bar{T}_{\text{eq}} - \Delta\bar{T}_{10})/\Delta\bar{T}_{\text{mean}}$ | $\Delta\bar{T}_{\text{mean}}$ (°C) |
|-----------------------|--------------------------------------|---|--|------------------------------------|
| CCCM/CGCM3.1(T63) | 0.83 | 0.40 | 0.18 | 2.26 |
| CCSR/MIROC3.2(medres) | 0.54 | 0.38 | 0.17 | 2.17 |
| CNRM/CM3 | 0.75 | 0.22 | 0.13 | 1.70 |
| GFDL/CM2.0 | 0.65 | 0.29 | 0.20 | 1.47 |
| GFDL/CM2.1 | 0.83 | 0.36 | 0.23 | 1.56 |
| GISS/EH | 0.66 | 0.32 | 0.17 | 1.92 |
| GISS/ER | -0.52 | -0.05 | -0.03 | 1.52 |
| IAP/FGOALS-g1.0 | 0.41 | 0.54 | 0.38 | 1.41 |
| INM/CM3.0 | 0.55 | 0.11 | 0.07 | 1.44 |
| IPSL/CM4 | 0.54 | 0.39 | 0.18 | 2.15 |
| MPI/ECHAM5 | 0.60 | 0.44 | 0.20 | 1.56 |
| MRI/CGCM2.3.2 | 0.81 | 0.31 | 0.10 | 3.09 |
| NCAR/CCSM3.0 | 0.50 | 0.53 | 0.27 | 1.98 |
| NCAR/PCM1 | 0.32 | 0.12 | 0.11 | 1.04 |
| MO/HadCM3 | 0.31 | 0.49 | 0.23 | 2.13 |

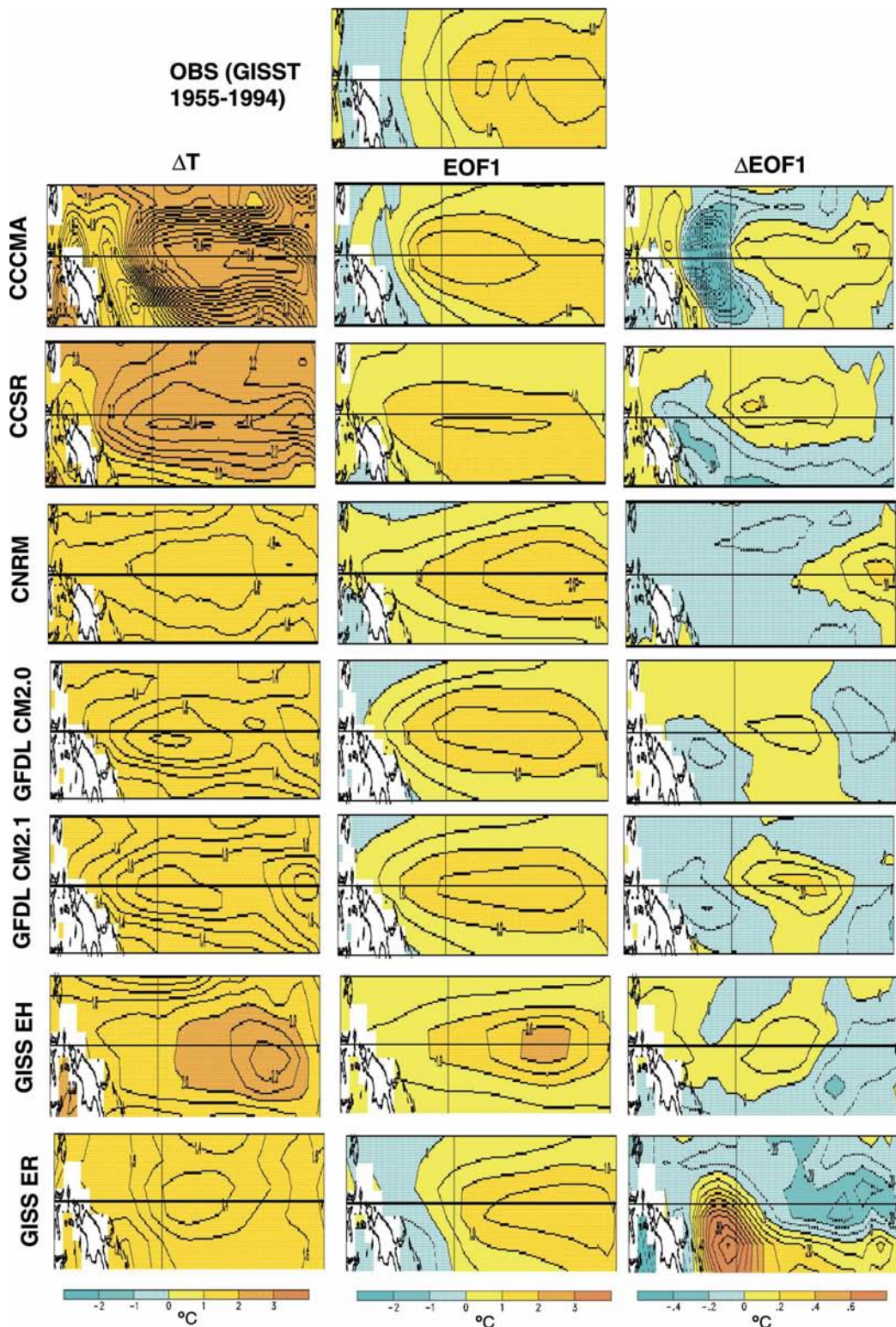


FIG. 3. (left) Mean increase $\Delta \bar{T}$ of SST in the near-equatorial Pacific (10°S – 10°N , 120°E – 90°W) for $2 \times \text{CO}_2$ relative to preindustrial climate. (center) Leading EOF1 for near-equatorial Pacific SST variability under preindustrial conditions. Spatial variance is normalized to unity. (right) Difference ΔEOF1 of EOF1, normalized similarly, for $2 \times \text{CO}_2$ climate minus that for preindustrial climate. Contour intervals are 0.5°C for EOF1, and 0.1°C for $\Delta \bar{T}$ and ΔEOF1 .

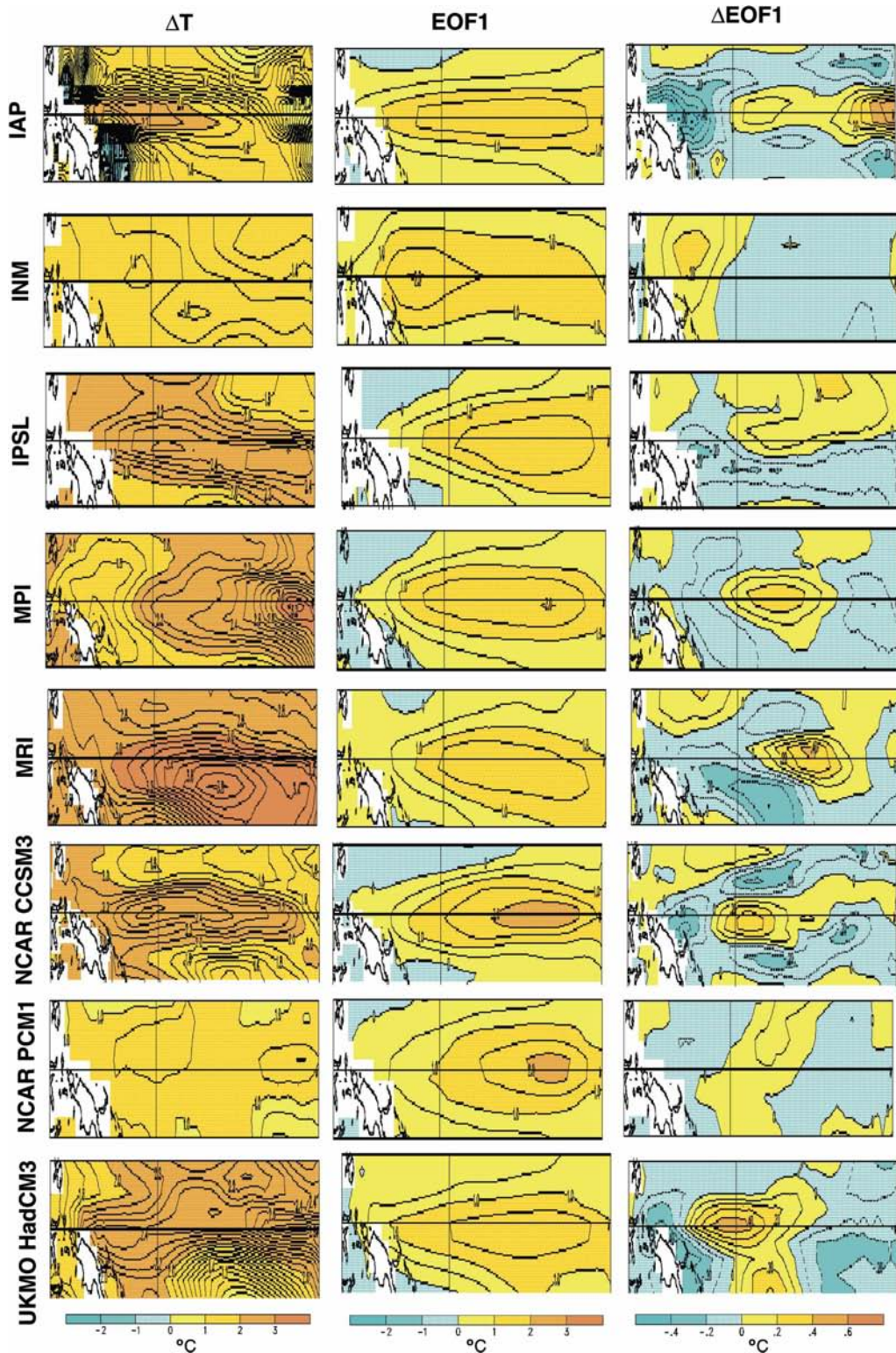


FIG. 3. (Continued)

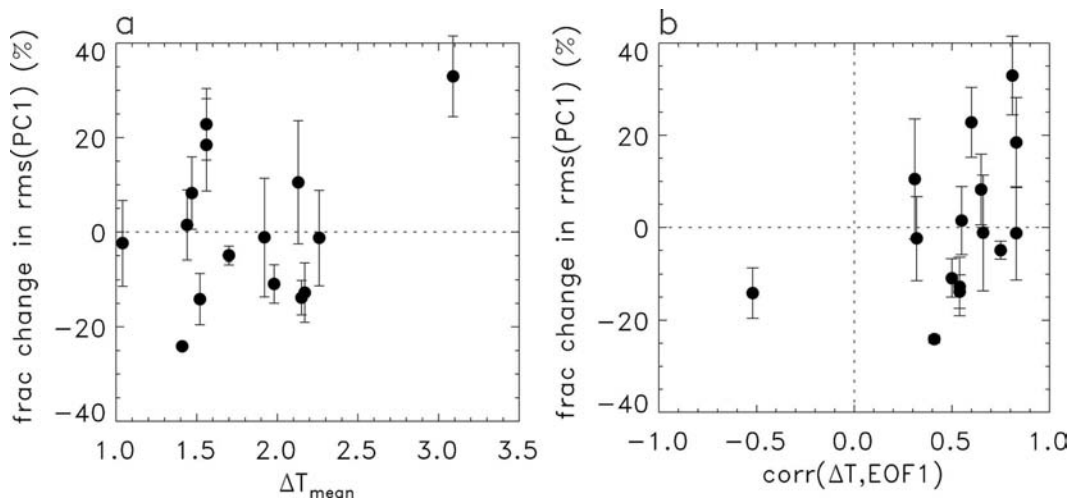


FIG. 4. (a) For each model the fractional change in ENSO amplitude, represented as the rms of PC1 vs $\Delta\bar{T}_{\text{mean}}$, the mean surface warming in the equatorial Pacific; (b) as in (a), but vs the spatial correlation between EOF1 and the warming pattern $\Delta\bar{T}$, both depicted in Fig. 3.

equatorial surface warming, not all show an ENSO amplitude increase.

While the ENSO amplitude increases described by Collins (2000a,b) in HadCM2 and in a version of HadCM3 subject to artificial equatorial warming were attributed to an intensified thermocline, these models also exhibited intensified near-equatorial meridional gradients in temperature, corresponding to particularly strong warming near the equator. There is some concentration of warming near the equator in most of the models considered here, as is evident in the first column of Fig. 3, which shows the spatial dependence of surface warming in the near-equatorial Pacific Ocean. Several measures quantifying this tendency are listed in Table 3. The first is the spatial correlation of the warming pattern $\Delta\bar{T}$ with EOF1. Because all EOF1 patterns are strongly concentrated near the equator, equatorially peaked warmings leading to increased meridional temperature gradients will be represented by strong positive correlations. As seen from Table 3, all models except one (GISS ER) exhibit positive correlations between 0.3 and 0.85, indicating that, by this measure at least, warming is “El Niño-like” (cf. Meehl and Washington 1996). [Of these, the lowest positive correlation is for UKMO HadCM3, consistent with the relatively weak response described in Collins (2000b).] This is somewhat in contrast with similar calculations by Collins et al. (2005) for 20 models submitted to the Coupled Model Intercomparison Project (CMIP). Among those models, most of which are older than those in the present group, seven showed negative correlations whereas only seven showed positive correlations

tions exceeding 0.3.⁴ In an earlier version of the Canadian Centre for Climate Modelling and Analysis (CCCMA) model, an El Niño-like warming pattern was found to be driven mainly by anomalous equatorward ocean heat transport (Yu and Boer 2002), whereas in two earlier NCAR models differences in eastward intensification of CO₂-induced warming were found to result from regional differences in cloud feedbacks (Meehl et al. 2000).

As an indication of whether such changes in meridional gradients might influence ENSO amplitude, ENSO amplitude changes are plotted in Fig. 4b against the spatial correlation between $\Delta\bar{T}$ and EOF1. Although there is some tendency for PC1 to increase when the spatial correlation is large and to remain stationary or decrease when it is small, the correlation coefficient describing this relationship is 0.44 (with or without the anomalous negative spatial correlation of model GISS ER), which is at best marginally significant (p – value ≈ 0.05 according to a one-sided t test). Additional measures in Table 3 that describe the tendency for ΔT to peak near the equator are $\Delta\bar{T}_{\text{eq}} - \Delta\bar{T}_{10}$, the difference between $\Delta\bar{T}$ zonally averaged at the equator and at $\pm 10^\circ$ latitude, and $(\Delta\bar{T}_{\text{eq}} - \Delta\bar{T}_{10})/\Delta\bar{T}_{\text{mean}}$, which is this difference expressed as a fraction

⁴ Methodological differences between the present study and Collins et al. (2005) include interpolation in the latter to a common 3.75° longitude by 2.5° latitude grid, as well as computation of warming patterns from linear trends during $1\% \text{ yr}^{-1}$ CO₂ increase rather than from stabilized $2 \times \text{CO}_2$ minus preindustrial differences.

TABLE 4. Quantities relating to the response τ'_x of zonal wind stress τ_x to ENSO-related SST perturbations, calculated as the regression of τ_x on PC1 of equatorial SST; x_{\max} is the longitude at which equatorial τ'_x attains its maximum $\max(\tau'_x)$, and Δy_τ is the half-width of the τ'_x pattern as defined by (1).

| Group/model | x_{\max} | $\max(\tau'_x)$ (Pa $^{\circ}\text{C}^{-1}$) | Δy_τ ($^{\circ}$) |
|-----------------------|------------------|--|--------------------------------|
| CCCMA/CGCM3.1(T63) | 165 $^{\circ}$ E | 0.26×10^{-1} | 4.8 |
| CCSR/MIROC3.2(medres) | 148 $^{\circ}$ E | 0.16×10^{-1} | 6.8 |
| CNRM/CM3 | 159 $^{\circ}$ W | 0.15×10^{-1} | 3.4 |
| GFDL/CM2.0 | 160 $^{\circ}$ E | 0.19×10^{-1} | 3.8 |
| GFDL/CM2.1 | 160 $^{\circ}$ E | 0.21×10^{-1} | 4.5 |
| GISS/EH | 155 $^{\circ}$ W | 0.11×10^{-1} | 3.3 |
| GISS/ER | 165 $^{\circ}$ W | 0.39×10^{-1} | 5.4 |
| IAP/FGOALS-g1.0 | 173 $^{\circ}$ W | 0.11×10^{-1} | 2.7 |
| INM/CM3.0 | 155 $^{\circ}$ W | 0.10×10^{-1} | 3.6 |
| IPSL/CM4 | 158 $^{\circ}$ W | 0.12×10^{-1} | 2.8 |
| MPI/ECHAM5 | 139 $^{\circ}$ E | 0.14×10^{-1} | 4.2 |
| MRI/CGCM2.3.2 | 179 $^{\circ}$ E | 0.29×10^{-1} | 4.7 |
| NCAR/CCSM3.0 | 179 $^{\circ}$ E | 0.16×10^{-1} | 2.8 |
| NCAR/PCM1 | 159 $^{\circ}$ W | 0.12×10^{-1} | 3.1 |
| MO/HadCM3 | 176 $^{\circ}$ E | 0.15×10^{-1} | 3.9 |
| GISST2 1955–1994 | 146 $^{\circ}$ W | 0.24×10^{-1} | 5.3 |

of the mean warming $\Delta \bar{T}_{\text{mean}}$ in the study region. These quantities exhibit less distinct relations to changes in ENSO amplitude than $\text{corr}(\Delta \bar{T}, \text{EOF1})$. Thus, changes in ENSO amplitude appear not to be clearly linked to changes in meridional SST gradient near the equator in the present set of models.

c. Influence of meridional extent of τ_x response

Another proposed influence on changes in ENSO amplitude is the meridional extent of the zonal wind stress response to anomalous equatorial SST, as discussed by Zelle et al. (2005) and in section 1 above. To quantify this meridional extent, regression patterns for zonal wind stress τ_x , indexed on time series of PC1, were computed for each control simulation as $\overline{\tau'_x \text{PC1}' / (\text{PC1}')^2}$, where the overbars denote temporal means and primes denote anomalies. The resulting regression patterns are very similar to those in Fig. 5 of Capotondi et al. (2006), and exhibit positive values peaking near the equator in the central and western Pacific, somewhat westward of the maximum SST variance as discussed, for example, by Zelle et al. (2005) and listed in Table 4. Taking into account this tendency, the width of the τ_x regression pattern is computed as the longitudinal average of

$$\Delta y_\tau = \left(\int \tau_x y^2 dy / \int \tau_x dy \right)^{1/2}, \quad (1)$$

within the Niño-4 longitude range 160 $^{\circ}$ E–150 $^{\circ}$ W, where y is latitude and the integration ranges from the equator

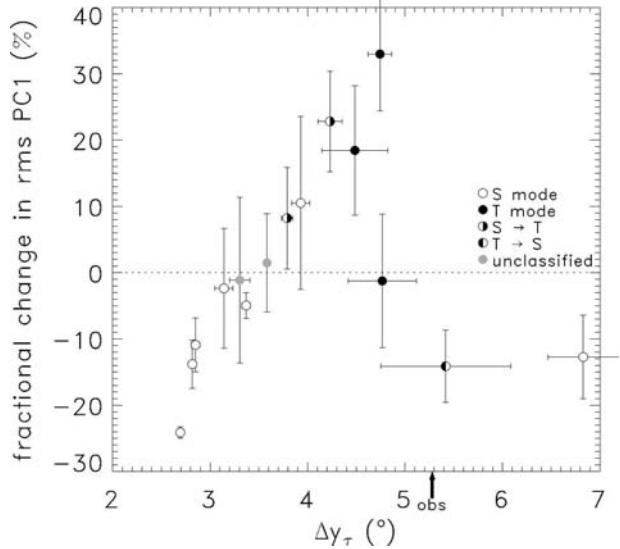


FIG. 5. Fractional changes in ENSO amplitude, as in Fig. 4, plotted against Δy_τ , the half-width of the τ_x regression pattern as defined by (1). The plotting symbols indicate whether the model ENSO has the character of an S mode or T mode as classified by Guilyardi (2006), with hybrid symbols denoting changes under CO_2 -induced warming as indicated (two of the models have not been so classified). The arrow indicates observational Δy_τ based on NCEP τ_x and GISST for 1955–94.

to northern and southern latitudes where τ_x either becomes negative or achieves a local minimum. Mean values for Δy_τ , averaged between century-long segments of the control runs, are given in Table 4. In Fig. 5, fractional changes in ENSO amplitude are plotted against Δy_τ , with error bars for the latter calculated as for other quantities. The models are divided essentially into two groups. The three models at lower right [CCCMA, Center for Climate System Research (CCSR), and GISS ER] all have relatively large Δy_τ and particularly weak ENSOs (Fig. 1; see also Fig. 3 of Guilyardi 2006). The remaining 12 models, which have ENSO amplitudes comparable to or greater than observed, follow a relatively tight, nearly linear relationship (correlation coefficient >0.97 , $p < 10^{-4}$), according to which models having a narrow τ_x response exhibit ENSO amplitude decreases, whereas models having a broader τ_x response exhibit increased ENSO amplitude under CO_2 doubling. Among these models the width of the τ_x response, and hence the degree to which ENSO amplitude decreases or increases, is in turn strongly dependent on whether SST variability arises mainly from local wind–SST feedback (S mode) or remote wind–thermocline feedback (T mode), according to classifications by Guilyardi (2006). [Several of the models change modes under CO_2 increase as indicated, whereas two were not classified in Guilyardi (2006).]

In discussing the influence of the width of the τ_x response on ENSO change, Zelle et al. (2005) emphasized that a narrow wind stress response is associated with both a stabler ENSO oscillation and a shorter period in simplified dynamical models (e.g., van der Vaart et al. 2000).⁵ They ascribed the insensitivity of ENSO to warming in CCSM1.4, which is not among the present collection of models, to a narrower τ_x response and hence stabler character as compared to observed ENSO. While a τ_x response width according to (1) has not been calculated here for CCSM1.4, the results in Fig. 5 suggest that the insensitivity found by Zelle et al. (2005) could have been due to the τ_x response width having a value near $\Delta\gamma_\tau \approx 3.5^\circ$, that is, between the regimes of amplitude decrease and increase in Fig. 5.

The observational value for $\Delta\gamma_\tau$, calculated using National Centers for Environmental Prediction (NCEP) τ_x and GISST data for 1955–94 and indicated in Fig. 5 by the arrow, is larger than $\Delta\gamma_\tau$ in any of the 12 models having realistically large ENSO amplitudes. This could be interpreted as suggesting that actual ENSO amplitude will increase under CO₂-induced warming. An alternative is to consider actual ENSO as having a hybrid character associated with apparent shifts between S-mode and T-mode behavior on multidecadal time scales (e.g., Guilyardi 2006). If such behavior is viewed as straddling the regimes of S-mode and T-mode behavior in Fig. 5, an amplitude increase under CO₂-induced warming is again suggested.

4. ENSO period

Power spectra of PC1 for observed SST and for each of the 15 models are shown in Fig. 6. The spectra are presented in variance-preserving form, that is, (frequency \times power) versus frequency, so that equal areas contribute equally to total variance. Blue curves correspond to preindustrial climate and associated standard deviations, and red curves to 2 \times CO₂ climate. Their differences (2 \times CO₂ – preindustrial) are indicated in black. Frequencies corresponding to the 25th and 75th percentiles of the observed spectrum are indicated by the vertical dashed lines. For most of the models, the peak in the power spectrum lies within this band. Exceptions include the CCSR, which exhibits too much

power at low frequencies, particularly under preindustrial conditions, and NCAR CCSM3.0, which exhibits too much power at high frequencies, particularly under 2 \times CO₂ conditions.

Changes in ENSO frequency under CO₂ doubling are quantified using a characteristic period corresponding to the centroid (50th percentile) of the power spectrum. In the case of the observed power spectrum, this characteristic period is 3.14 yr. Values for each of the models under preindustrial and 2 \times CO₂ conditions are listed in Table 5. In Fig. 7 characteristic periods for preindustrial climate are plotted against those for 2 \times CO₂ climate. Points lying above the line having unit slope indicate decreases in characteristic ENSO period under CO₂ doubling; this is the case for 12 of the 15 models. Of the remaining three models, GFDL CM2.0 and UKMO HadCM3 exhibit period increases that are less than two standard deviations of the preindustrial sample. Only the MRI model exhibits a period increase that is larger. The mean fractional decrease for all the models is 4.6% and remains between 2.7% and 4.2% if the four models exhibiting the largest fractional period changes are successively excluded.

In Fig. 8 these period changes are shown in units of bias-corrected standard deviations obtained from the preindustrial control sample. An overall tendency for ENSO period to decrease is again evident. As in Fig. 2, if the period differences were a result of sampling normally distributed intercentennial variations in period, the histogram would sample the 1 σ -wide Gaussian (thin curve) if σ were well known, and a *t*-distribution (thick curve, extreme case for $N_{\text{PICTL}} = 3$) in the present case where σ must be estimated. The distribution is again skewed by outlying results arising from three realizations of the IAP model, for which σ is very small. Application of two-sided *t* tests to the individual models indicates that these shifts are significant at $p < 0.1$ in only five cases. However, a difference-in-means *t* test applied to all the models except outlying IAP indicates that the shift in ensemble mean is significant at $p = (0.08, 0.05, 0.03)$ taking degrees of freedom = (2, 3, 4).

Many factors can affect the period of ENSO, including nonlinearity (Münnich et al. 1991; Eccles and Tziperman 2004), the strengths of various feedbacks on SST (e.g., Battisti and Hirst 1989), the latitudinal breadth of zonal wind stress response to equatorial SST perturbations (Kirtman 1997; van der Vaart et al. 2000), and the efficiency with which Rossby and Kelvin waves are reflected at the western and eastern boundaries (Kang and An 1998). Collins (2000a,b) argued that a period decrease found under 4 \times CO₂ conditions in HadCM2 and in versions of HadCM2 and HadCM3 forced by artificially imposed heat fluxes near the equa-

⁵ The latter relationship was also found by Kirtman (1997) using a dynamical ocean model coupled to a statistical atmosphere in which the τ_x response pattern was assigned differing widths. Among the present models, $\Delta\gamma_\tau$ and ENSO period are related less clearly (correlation coefficient = 0.77), and plotting ENSO amplitude change against ENSO period produces a less distinct relation than that in Fig. 5.

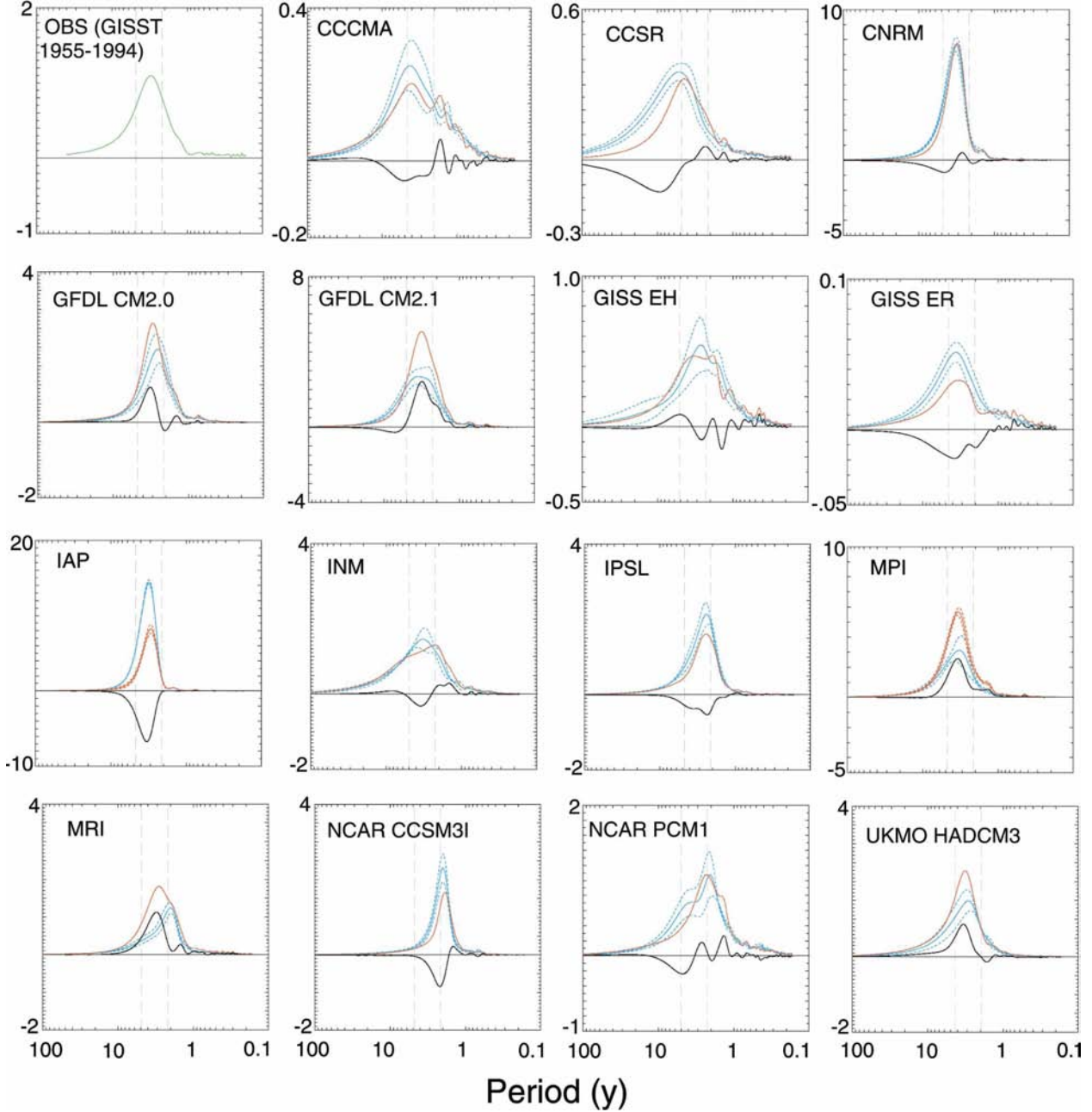


FIG. 6. Variance-preserving power spectra (power \times frequency vs frequency) of PC1 for (first panel) 1955–94 GISST observations and (remaining panels) coupled models. Mean spectra for preindustrial climates, based on samples of centennial monthly time series, are blue and those for stabilized $2 \times \text{CO}_2$ climates are red; their differences are plotted in black. Standard deviations in cases where the sample size is ≥ 3 are indicated by the dashed curves. Vertical dashed lines indicate periods corresponding to 25th and 75th percentiles of observed power spectrum. Spectra are smoothed using a 24-bin Parzen window.

tor could be the result of enhanced near-equatorial meridional temperature gradients, as these reduce the time scale for changes in equatorial heat content anomaly, which governs ENSO period in the recharge oscillator description of Jin (1997). However, no strong correspondence was found here between ENSO period

changes and the changes in near-equatorial meridional SST gradient listed in Table 3.

Another factor that can affect ENSO period under the delayed oscillator paradigm (Suarez and Schopf 1988; Battisti and Hirst 1989; see also discussion in Neelin et al. 1998) is the time delay by which equatorial

TABLE 5. Characteristic ENSO period in years, calculated as centroid of the PC1 power spectrum, for preindustrial and $2 \times \text{CO}_2$ climates. Uncertainties represent standard deviations obtained from samples of centennial time series in cases where sample size $N \geq 3$; p values are the probabilities that differences as large or larger arise through random sampling from a normal distribution.

| Group/model | P_{PICTL} (yr) | $P_{2 \times \text{CO}_2}$ (yr) | Change (%) | p value |
|-----------------------|-------------------------|---------------------------------|--------------|-----------|
| CCCMA/CGCM3.1(T63) | 3.82 ± 0.20 | 3.77 | -1 ± 5 | >0.2 |
| CCSR/MIROC3.2(medres) | 6.22 ± 0.57 | 4.33 | -30 ± 9 | 0.03 |
| CNRM/CM3 | 3.44 ± 0.11 | 3.25 | -6 ± 3 | 0.18 |
| GFDL/CM2.0 | 2.70 ± 0.22 | 2.95 | 8 ± 8 | >0.2 |
| GFDL/CM2.1 | 3.53 ± 0.14 | 3.13 | -11 ± 4 | 0.05 |
| GISS/EH | 3.02 ± 0.80 | 2.94 | -3 ± 27 | >0.2 |
| GISS/ER | 3.82 ± 0.42 | 3.32 | -13 ± 11 | >0.2 |
| IAP/FGOALS-g1.0 | 3.29 ± 0.01 | 3.10 ± 0.04 | -6 ± 1 | <0.01 |
| INM/CM3.0 | 3.72 ± 0.06 | 3.63 | -3 ± 2 | >0.2 |
| IPSL/CM4 | 2.72 ± 0.14 | 2.64 | -3 ± 5 | >0.2 |
| MPI/ECHAM5 | 3.72 ± 0.35 | 3.46 ± 0.07 | -7 ± 10 | >0.2 |
| MRI/CGCM2.3.2 | 2.39 ± 0.10 | 2.79 | 17 ± 4 | 0.06 |
| NCAR/CCSM3.0 | 2.13 ± 0.06 | 1.96 | -8 ± 3 | 0.03 |
| NCAR/PCM1 | 2.59 ± 0.29 | 2.40 | -8 ± 11 | >0.2 |
| MO/HadCM3 | 3.38 ± 0.34 | 3.56 | 5 ± 10 | >0.2 |

waves provide delayed negative feedback. This delay is determined by the propagation speeds of equatorial Kelvin and Rossby waves, which in turn are proportional to the baroclinic gravity wave phase speed near the equator. The baroclinic gravity wave phase speed

scales, under the WKB approximation, as the integral of buoyancy frequency through the water column (Chelton et al. 1998). Thus, if stratification of the upper ocean increases because of near-surface warming, as for example in Timmermann et al. (1999) or Collins (2000a), the equatorial wave speed should also increase. Such changes have been evaluated for several of the models considered here by Saenko (2006), who finds that each exhibits a comparable (to within a factor of 2) increase in zonally averaged near-equatorial gravity wave speed. Under the A1B scenario for greenhouse gas emissions, in which CO_2 increases to 720 ppm or 2.5 times preindustrial CO_2 and then stabilizes, the mean increase in gravity wave speed at the end of the first century following stabilization is 13.7%. To enable an approximate scaling of this result to the present context of wave speed change in the equatorial Pacific under CO_2 doubling, the latter was estimated for one model (GFDL CM2.0) by comparing wave speed averaged over the first and tenth decades following $2 \times \text{CO}_2$ stabilization with a comparable period in the preindustrial control run (O. Saenko 2005, personal communication). The resulting wave speed increase is 4.5%, about 0.4 times that found for the same model under the higher CO_2 conditions considered in Saenko (2006). Scaling the 13.7% mean increase among all the models considered by Saenko (2006) by this ratio yields an estimated mean increase in the present case of 5.6%, comparable to the ENSO period decrease reported above. This result is consistent with delayed oscillator theory, under which decreased wave propagation time leads to decreased ENSO period, with fractional changes in these two time scales that, while not identical, are generally similar in magnitude (e.g., Fig. 17b of

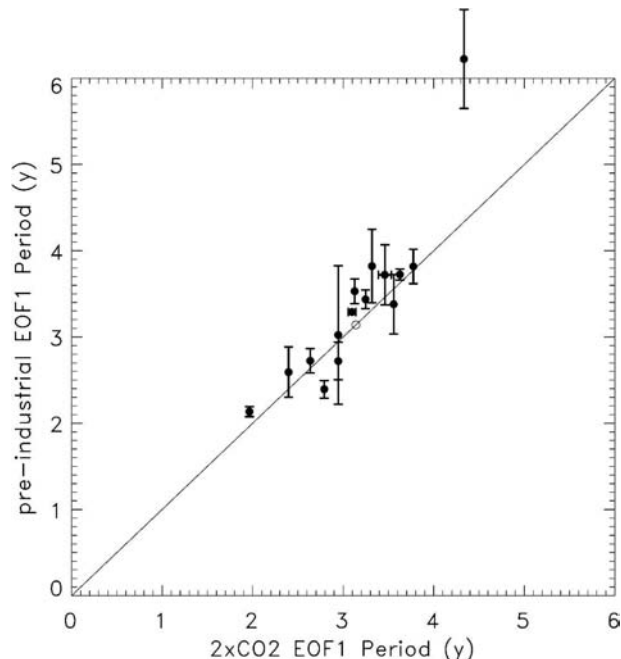


FIG. 7. Characteristic ENSO period, calculated for each centennial time series as the centroid of the smoothed PC1 power spectrum, for preindustrial climate (vertical axis) and $2 \times \text{CO}_2$ climate (horizontal axis). Error bars indicate ± 1 std dev as evaluated from samples of centennial time series. The open circle denotes the characteristic period obtained via this procedure for observed monthly SST (GISST 1955–94).

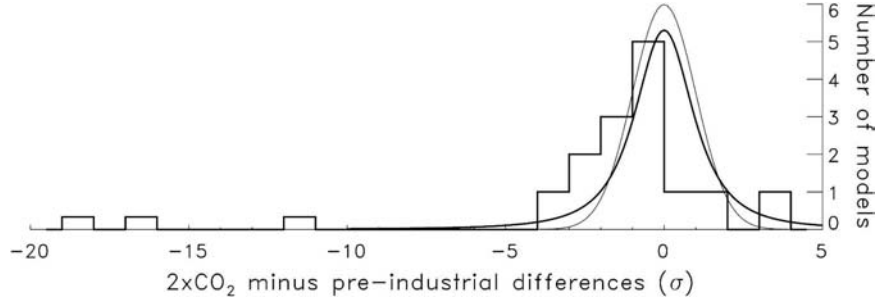


FIG. 8. Histogram of changes ($2 \times \text{CO}_2$ minus preindustrial) in characteristic ENSO period as plotted in Fig. 7, for the 15 models in units of standard deviations σ estimated from preindustrial centennial time series. As in Fig. 2, each realization is assigned a weight $1/N_{2 \times \text{CO}_2}$, where $N_{2 \times \text{CO}_2}$ is the number of $2 \times \text{CO}_2$ realizations. If the centennially sampled preindustrial periods were distributed normally and ENSO did not change under CO_2 doubling, the histograms would tend toward normal distributions (thin curves) if the σ were known exactly, and toward two-degrees-of-freedom t distributions (thick curves) if all σ were estimated from $N_{\text{PICTL}} = 3$ samples.

Battisti and Hirst 1989 and Fig. 3 of Suarez and Schopf 1988).

While other influences doubtless enter that may either increase or decrease ENSO period, this increase in equatorial wave speed, which must occur in all models based on the simple consideration that surface warming leads that of the deeper ocean, should act as a bias toward shorter period, and therefore is a plausible explanation for the tendency for ENSO periods to decrease as illustrated in Figs. 7 and 8.

5. ENSO pattern

Changes in the ENSO pattern, defined as differences ΔEOF1 between comparably normalized EOF1 for $2 \times \text{CO}_2$ and preindustrial climates, exhibit a range of forms, shown in the right-hand column of Fig. 3. In many of the models ΔEOF1 is negative in the eastern and/or western equatorial Pacific, and positive, implying a relative intensification of SST variability, in the central equatorial Pacific. In comparing ΔEOF1 with the SST warming pattern $\Delta\bar{T}$ in the first column of Fig. 3, it appears that the largest positive values of ΔEOF1 often coincide with large $\Delta\bar{T}$ or with negative changes in the zonal SST gradient $\Delta\bar{T}_x$; the latter reflect a strengthening of the generally negative ambient zonal SST gradient (SST decreasing from west to east). On the other hand, the largest negative ΔEOF1 often coincide with locales of positive $\Delta\bar{T}_x$, where the ambient zonal SST gradient has weakened.

These apparent tendencies motivate the following interpretation of the ΔEOF1 patterns. ENSO-related variations in equatorial SST are driven primarily by three feedbacks, as described by Dijkstra and Burgers

(2002). These are 1) anomalous zonal advection of mean zonal temperature gradients, or zonal-advective feedback; 2) anomalous vertical advection of mean vertical temperature gradients, or upwelling feedback; and 3) advection of subsurface temperature anomalies by mean vertical velocity, or thermocline feedback. Evolution of SST anomalies T' can thus approximately be described by

$$\frac{\partial T'}{\partial t} \approx -u'\bar{T}_x - w'\frac{(\bar{T} - \bar{T}_S)}{H} - \bar{w}\frac{(T' - T'_S)}{H} + \text{advection of anomalies} + \text{damping}, \quad (2)$$

where u and w are the zonal and upwelling velocity, respectively, T_x is the zonal SST gradient, T_S is the subsurface temperature at depths from which water upwells, H is a length scale for which $(T' - T'_S)/H$ approximates vertical temperature gradient beneath the mixed layer, and the overbars and primes denote mean and anomalous quantities.

Viewing (2) as determining the pattern of SST variability, changes under a perturbed climate such as the $2 \times \text{CO}_2$ climates considered here are next examined. Changes in the SST feedback terms in (2) will result from (i) changes in the velocity and subsurface temperature anomalies, assumed in a first approximation to be described by $\varepsilon u'$, $\varepsilon w'$, and $\varepsilon T'_S$, that is, by an overall shift in amplitude; (ii) changes in the mean temperature structure, with perturbations to zonal mean temperature gradient denoted by $\Delta\bar{T}_x$ and to surface-subsurface temperature difference by $\Delta(\bar{T} - \bar{T}_S)$; and (iii) changes in the mean upwelling velocity $\Delta\bar{w}$. Assuming such changes to be relatively small, so that terms quadratic in the perturbations can be neglected, and denoting by T'_1 ,

T'_2 , and T'_3 the respective modifications to the SST anomaly pattern due to these effects, we have

$$\frac{\partial T'_1}{\partial t} \approx -\varepsilon u' \bar{T}_x - \varepsilon w' \frac{(\bar{T} - \bar{T}_S)}{H} - \frac{w'}{H} \frac{(T'_1 - \varepsilon T'_S)}{H} + \dots, \quad (3)$$

$$\frac{\partial T'_2}{\partial t} \approx -u' \Delta \bar{T}_x - w' \frac{\Delta(\bar{T} - \bar{T}_S)}{H} + \dots, \quad (4)$$

$$\frac{\partial T'_3}{\partial t} \approx -\Delta \bar{w} \frac{\Delta(T' - T'_S)}{H} + \dots, \quad (5)$$

where “ \dots ” denotes perturbed advection and damping terms, to which similar considerations apply. According to (2) and (3), T'_1 obeys the same physics as T' , and hence represents simply an increase or decrease in anomaly amplitude, depending on the sign of ε . Such changes will influence PC1 variance, but do not affect the normalized EOF1 pattern and hence will not contribute to ΔEOF1 . In the case of T'_2 it is seen from (2) and (4) that generation of SST anomalies by the zonal advection feedback is intensified where $\Delta \bar{T}_x < 0$ reinforces the (mainly negative) unperturbed gradient \bar{T}_x , and diminished where $\Delta \bar{T}_x > 0$. In addition, generation of SST anomalies by the upwelling feedback is intensified if $\Delta(\bar{T} - \bar{T}_S) > 0$, as occurs during or immediately following a period of climatic warming when there is a lag between surface and subsurface warming (e.g., Timmermann et al. 1999). Finally, T'_3 describes, according to (5), an increase or decrease in the thermocline feedback due to changes in $\Delta \bar{w}$.

If, as suggested by the preceding analysis, changes to the pattern of SST variability in a perturbed climate are governed at least partly by mean SST changes (insight into additional influences due to changes in mean subsurface temperature $\Delta \bar{T}_S$ and in $\Delta \bar{w}$ could be gained through analysis of subsurface ocean model output, which is not attempted here), a tendency should exist for ΔEOF1 to be governed by zonal advection of the anomalous temperature gradient $\Delta \bar{T}_x$ in regions where $|\Delta \bar{T}_x|$ is large. In regions where $|\Delta \bar{T}_x|$ is small, surface-intensified warming described by $\Delta \bar{T} > 0$ should locally enhance ENSO amplitude ($\Delta\text{EOF1} > 0$) through advection of the anomalous vertical temperature gradient. These tendencies, described by the last two terms in (4), are consistent with the apparent tendencies, noted at the beginning of this section, for large negative ΔEOF1 to coincide with positive $\Delta \bar{T}_x$ and large positive ΔEOF1 to coincide with negative $\Delta \bar{T}_x$ or large $\Delta \bar{T}$.

These relationships are illustrated in Fig. 9, where $\Delta \bar{T}_x$ and $\Delta \bar{T}$ are plotted for grid cells belonging to the lowest quartile of ΔEOF1 (open circles) and to the highest quartile (filled circles) for four models, chosen

to represent a range of behaviors typifying the full ensemble. The dotted lines denote \pm one-half of rms $\Delta \bar{T}_x$, and divide the plane into regions having strong negative $\Delta \bar{T}_x$, weak $|\Delta \bar{T}_x|$, and strong positive $\Delta \bar{T}_x$. In three of these four models (CCCMA, GFDL 2.1, and UKMO HadCM3) negative ΔEOF1 are predominant where $\Delta \bar{T}_x > 0$, whereas positive ΔEOF1 are prevalent where $\Delta \bar{T}_x < 0$ and (less obviously) $|\Delta \bar{T}_x| \approx 0$, precisely as expected from (4). In the fourth model, CNRM, any such relation is much less evident; the fact that ΔEOF1 is concentrated in the far eastern Pacific, where the thermocline feedback generally dominates (Burgers and van Oldenborgh 2003; van Oldenborgh et al. 2005) suggests that the modification to this feedback through changes in mean upwelling, described by (5), may be important in this case.

The preceding analysis is extended to all of the models in Table 6, which tabulates the numbers N^- of first quartile ΔEOF1 and N^+ of fourth quartile ΔEOF1 in each of the aforementioned regions of the $\Delta \bar{T} - \Delta \bar{T}_x$ plane. Pairs in boldface obey $N^+ > N^-$ for $\Delta \bar{T}_x < 0$ and $|\Delta \bar{T}_x| \approx 0$, and $N^+ < N^-$ for $\Delta \bar{T}_x > 0$, indicative of the influence of $\Delta \bar{T}$ on ΔEOF1 described by (4). Such a relation holds in 42 of 45 cases, with exceptions occurring for the CNRM and IAP models, for which ΔEOF1 is concentrated in the far eastern Pacific where the effect described by (5) may dominate, and for the GISS EH model, which, unique among the considered models, employs a hybrid vertical coordinate that is primarily isopycnal beneath the mixed layer and may influence its representation of equatorial upwelling. These results appear to confirm that, in most models, changes to EOF1 under CO_2 doubling can be understood at least partly as resulting from the impact of warming-induced changes in SST on advective generation of SST anomalies as described by (4).

6. Discussion and conclusions

Sensitivity of ENSO-like variability to increased atmospheric CO_2 has been examined through EOF analyses of 15 coupled climate models evaluated for the IPCC Fourth Assessment Report. Differences in ENSO amplitude, period, and pattern between a low- CO_2 (preindustrial) control climate and a climate in which CO_2 has stabilized at twice its preindustrial concentration are considered. To distinguish between changes to ENSO caused by climatic warming and modulations that occur in the absence of forced climate change, these differences are compared against changes to ENSO that occur within the multicentury control runs.

Under control conditions the models exhibit a broad

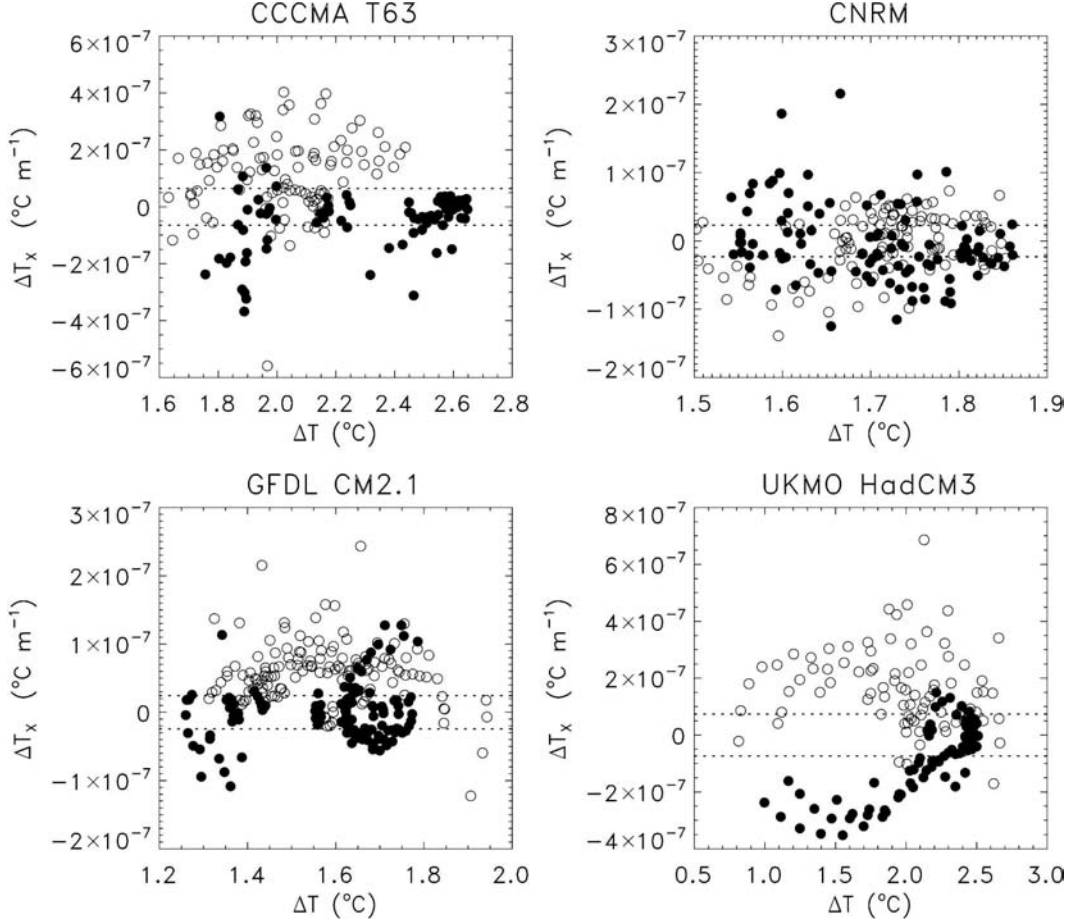


FIG. 9. Properties of changes ΔEOF1 to EOF1 , shown in Fig. 3, under CO_2 doubling for four representative models. Each symbol represents $\Delta\bar{T}$ (also shown in Fig. 3) and $\Delta\bar{T}_x$ at an equatorial Pacific grid location. Open circles denote points belonging to the lowest quartile of ΔEOF1 (ΔEOF1 generally <0), and filled circles denote points belonging to the highest quartile (ΔEOF1 generally >0). The dashed lines bracket values of $\Delta\bar{T}_x$ less than half its rms, and divide the plane into three regions having significantly negative $\Delta\bar{T}_x$, small $|\Delta\bar{T}_x|$, and significantly positive $\Delta\bar{T}_x$. In Table 6 the numbers N^+ and N^- of filled and open circles lying within each of these three regions are listed for each of the 15 models. The distributions are consistent (with possible exceptions of CNRM, GISS EH, and IAP models) with ΔEOF1 being controlled by $\Delta\bar{T}_x$ where $|\Delta\bar{T}_x|$ is large, and by surface warming $\Delta\bar{T}$ elsewhere through the mechanisms discussed in section 5.

range of ENSO-like behavior, with most displaying ENSO amplitudes comparable to or greater than that observed in the second half of the twentieth century. Characteristic periods, which range within a factor of 2 or so, are approximately centered on the observed period.

Under CO_2 doubling, 8 of the 15 models exhibit ENSO amplitude changes that significantly ($p < 0.1$) exceed centennial time scale variability within the respective control runs. However, in five of these models the amplitude decreases whereas in three it increases; hence there is no consensus as to the sign of change. While the amplitude changes are not strongly related to the magnitude or pattern of surface warming, a rela-

tionship is evident between amplitude change and the meridional width of the zonal wind stress response in the 12 models whose ENSO amplitudes are comparable to or larger than observed. The implied relation is that a narrow (wide) wind stress response is associated with ENSO amplitude decrease (increase). It is further noted that a narrow wind stress response and amplitude decrease occurs mainly in models whose ENSO is dominated by SST feedbacks as classified by Guilyardi (2006), whereas a wide wind stress response and amplitude increase occurs mainly in models whose ENSO is dominated by thermocline feedbacks.

The intercomparison yields a more consistent picture with respect to changes in period, with four models

TABLE 6. Statistics of $\Delta\text{EOF1}(x, y)$, the change under CO₂ doubling in the leading EOF of tropical Pacific SST, binned according to local $\Delta\bar{T}_x(x, y)$, the change in zonal SST gradient under CO₂ doubling (see Fig. 9). For each bin, N^+ denotes the number of grid cells having ΔEOF1 in the highest quartile (largest positive values of ΔEOF1), and N^- the number of cells having ΔEOF1 in the lowest quartile (largest negative ΔEOF1). Entries in boldface are consistent with the hypothesis discussed in section 5 that changes in EOF1 are related inversely to changes in zonal temperature gradient and, secondarily, to changes in SST.

| Group/model | Bin | | | | | |
|-----------------------|-----------------------|------------|-----------------------------|------------|-----------------------|------------|
| | $\Delta\bar{T}_x < 0$ | | $\Delta\bar{T}_x \approx 0$ | | $\Delta\bar{T}_x > 0$ | |
| | N^+ | N^- | N^+ | N^- | N^+ | N^- |
| CCCMA/CGCM3.1(T63) | 23 | 9 | 73 | 32 | 4 | 59 |
| CCSR/MIROC3.2(medres) | 24 | 4 | 74 | 56 | 4 | 42 |
| CNRM/CM3 | 41 | 31 | 37 | 37 | 25 | 35 |
| GFDL/CM2.0 | 61 | 16 | 61 | 32 | 11 | 85 |
| GFDL/CM2.1 | 44 | 2 | 68 | 25 | 21 | 106 |
| GISS/EH | 5 | 14 | 32 | 19 | 5 | 9 |
| GISS/ER | 22 | 4 | 20 | 15 | 0 | 23 |
| IAP/FGOALS-g1.0 | 6 | 10 | 84 | 74 | 4 | 10 |
| INM/CM3.0 | 13 | 4 | 14 | 12 | 8 | 19 |
| IPSL/CM4 | 37 | 5 | 23 | 14 | 9 | 50 |
| MPI/ECHAM5 | 48 | 9 | 115 | 69 | 71 | 156 |
| MRI/CGCM2.3.2 | 25 | 6 | 65 | 38 | 12 | 58 |
| NCAR/CCSM3.0 | 126 | 103 | 23 | 187 | 29 | 104 |
| NCAR/PCM1 | 38 | 12 | 43 | 39 | 14 | 44 |
| UKMO/HadCM3 | 38 | 3 | 42 | 22 | 6 | 61 |

showing $p < 0.1$ decreases, and only one showing such an increase. The mean period decrease for all models of about 5% appears comparable in magnitude to the increase in equatorial wave speed caused by the enhancement of stratification resulting from the surface-intensified nature of ocean warming as discussed by Saenko (2006). This result appears compatible with delayed-oscillator descriptions of ENSO, in which the ENSO period is at least partly determined by time delays associated with propagation of equatorial waves.

Changes in the pattern of tropical Pacific SST variability as described by the (normalized) leading EOF show a range of behaviors, with more than half of the models exhibiting a pronounced intensification in the central Pacific and two exhibiting an intensification in the far eastern Pacific. These changes in the leading EOF appear to be at least partly attributable to anomalous zonal and vertical advection associated with warming-induced changes in SST, although subsurface effects such as those discussed by Meehl et al. (2006) are not considered in this analysis.

Because the models vary widely in their ability to simulate present-day ENSO, their associated predictions of warming-induced changes cannot be viewed as equally reliable. Five of the models considered here

were found by van Oldenborgh et al. (2005) to exhibit reasonably realistic balances of ENSO feedbacks and on this basis were considered as yielding the most reliable forecasts. However, restricting attention to these models does not substantially narrow the spread in projected ENSO changes. Amongst this subset, one model (CCSR) shows at best a marginally significant ($p = 0.12$) amplitude decrease, two (GFDL CM2.1 and MPI) show a $p \leq 0.1$ increase, and the remaining two (GFDL CM2.0 and UKMO HadCM3) show a modest but non-statistically significant increase. With respect to period changes, $p < 0.1$ decreases occur in CCSR and GFDL CM2.1, whereas in GFDL CM2.0, MPI, and UKMO HadCM3 the period changes are not significant. One aspect of ENSO change that these five models do have in common is that all exhibit a relative intensification of SST variability in the central Pacific that is consistent with anomalous zonal and vertical advection resulting from warming-induced changes in SST as discussed in section 5.

Acknowledgments. Slava Kharin, Steve Lambert, Geert Jan van Oldenborgh, Gerry Meehl, and an anonymous reviewer are thanked for suggesting improvements to the manuscript. The essential contributions of the international modeling groups that provided their data for analysis; the Program for Climate Model Diagnosis and Intercomparison (PCMDI), which collected and archived the model data; the JSC/CLIVAR Working Group on Coupled Modelling (WGCM) and their Coupled Model Intercomparison Project (CMIP) and Climate Simulation Panel, which organized the model data analysis activity; and the IPCC WGI TSU, which provided technical support, are gratefully acknowledged. The IPCC Data Archive at Lawrence Livermore National Laboratory is supported by the Office of Science, U.S. Department of Energy.

REFERENCES

- Battisti, D. S., and A. C. Hirst, 1989: Interannual variability in a tropical atmosphere-ocean model: Influence of the basic state, ocean geometry and nonlinearity. *J. Atmos. Sci.*, **46**, 1687–1712.
- Burgers, G., and G. J. van Oldenborgh, 2003: On the impact of local feedbacks in the central Pacific on the ENSO cycle. *J. Climate*, **16**, 2396–2407.
- Capotondi, A., A. Wittenberg, and S. Masina, 2006: Spatial and temporal structure of Tropical Pacific interannual variability in 20th century coupled simulations. *Ocean Model.*, in press.
- Chelton, D. B., R. A. deSzoeke, M. G. Schlax, K. El Naggar, and N. Siwertz, 1998: Geographical variability of the first-baroclinic Rossby radius of deformation. *J. Phys. Oceanogr.*, **28**, 433–460.
- Collins, M., 2000a: The El Niño-Southern Oscillation in the Sec-

- ond Hadley Centre Coupled Model and its response to greenhouse warming. *J. Climate*, **13**, 1299–1312.
- , 2000b: Understanding uncertainties in the response of ENSO to greenhouse warming. *Geophys. Res. Lett.*, **27**, 3509–3512.
- , and the CMIP Modelling Groups, 2005: El Niño- or La Niña-like climate change? *Climate Dyn.*, **24**, 89–104.
- Dijkstra, H. A., and G. Burgers, 2002: Fluid mechanics of El Niño variability. *Annu. Rev. Fluid Mech.*, **34**, 531–558.
- Eccles, F., and E. Tziperman, 2004: Nonlinear effects on ENSO's period. *J. Atmos. Sci.*, **61**, 474–482.
- Guilyardi, E., 2006: El Niño-mean state–seasonal cycle interactions in a multi-model ensemble. *Climate Dyn.*, **26**, 329–348.
- Jin, F.-F., 1997: An equatorial ocean recharge paradigm for ENSO. Part I: Conceptual model. *J. Atmos. Sci.*, **54**, 811–829.
- Kang, I.-S., and S.-I. An, 1998: Kelvin and Rossby wave contributions to the SST oscillation of ENSO. *J. Climate*, **11**, 2461–2469.
- Kirtman, B. P., 1997: Oceanic Rossby wave dynamics and the ENSO period in a coupled model. *J. Climate*, **10**, 1690–1704.
- Knutson, T. R., and S. Manabe, 1994: Impact of increased CO₂ on simulated ENSO-like phenomena. *Geophys. Res. Lett.*, **21**, 2295–2298.
- , and —, 1998: Model assessment of decadal variability and trends in the tropical Pacific Ocean. *J. Climate*, **11**, 2273–2296.
- , —, and D. Gu, 1997: Simulated ENSO in a global coupled ocean–atmosphere model: Multidecadal amplitude modulation and CO₂ sensitivity. *J. Climate*, **10**, 138–161.
- Monahan, A. H., 2001: Nonlinear principal component analysis: Tropical Indo-Pacific sea surface temperature and sea level pressure. *J. Climate*, **14**, 219–233.
- , and A. Dai, 2004: The spatial and temporal structure of ENSO nonlinearity. *J. Climate*, **17**, 3026–3036.
- Meehl, G. A., and W. M. Washington, 1996: El Niño-like climate change in a model with increased CO₂ concentrations. *Nature*, **382**, 56–60.
- , G. W. Branstator, and W. M. Washington, 1993: Tropical Pacific interannual variability and CO₂ climate change. *J. Climate*, **6**, 42–63.
- , W. D. Collins, B. Boville, J. T. Kiehl, T. M. L. Wigley, and J. M. Arblaster, 2000: Response of the NCAR Climate System Model to increased CO₂ and the role of physical processes. *J. Climate*, **13**, 1879–1898.
- , H. Teng, and G. W. Branstator, 2006: Future changes of El Niño in two global coupled climate models. *Climate Dyn.*, **26**, 549–566.
- Münnich, M., M. A. Cane, and S. E. Zebiak, 1991: A study of self-excited oscillations of the tropical ocean–atmosphere system. Part II: Nonlinear cases. *J. Atmos. Sci.*, **48**, 1238–1248.
- Neelin, J. D., D. S. Battisti, A. C. Hirst, F.-F. Jin, Y. Wakata, T. Yamagata, and S. E. Zebiak, 1998: ENSO theory. *J. Geophys. Res.*, **103**, 14 261–14 290.
- Saenko, O. A., 2006: Influence of global warming on baroclinic Rossby radius in the ocean: A model intercomparison. *J. Climate*, **19**, 1354–1360.
- Suarez, M. J., and P. S. Schopf, 1988: A delayed action oscillator for ENSO. *J. Atmos. Sci.*, **45**, 3283–3287.
- Tett, S., 1995: Simulation of El Niño–Southern Oscillation-like variability in a global AOGCM and its response to CO₂ increase. *J. Climate*, **8**, 1473–1502.
- Timmermann, A., M. Latif, A. Bacher, J. Oberhuber, and E. Roeckner, 1999: Increased El Niño frequency in a climate model forced by future greenhouse warming. *Nature*, **398**, 694–696.
- Tudhope, A. W., and Coauthors, 2001: Variability in the El Niño–Southern Oscillation through a glacial–interglacial cycle. *Science*, **291**, 1511–1517.
- van der Vaart, P. C. F., H. A. Dijkstra, and F.-F. Jin, 2000: The Pacific cold tongue and the ENSO mode: A unified theory within the Zebiak–Cane model. *J. Atmos. Sci.*, **57**, 967–988.
- van Oldenborgh, G. J., S. Y. Philip, and M. Collins, 2005: El Niño in a changing climate: A multi-model study. *Ocean Sci.*, **1**, 81–95.
- von Storch, H., and F. W. Zwiers, 1999: *Statistical Analysis in Climate Research*. Cambridge University Press, 528 pp.
- Wang, B., and S.-I. An, 2001: Why the properties of El Niño changed during the late 1970s. *Geophys. Res. Lett.*, **28**, 3709–3712.
- Yu, B., and G. J. Boer, 2002: The roles of radiation and dynamical processes in the El Niño-like response to global warming. *Climate Dyn.*, **19**, 539–554.
- Zelle, H., G. J. van Oldenborgh, G. Burgers, and H. Dijkstra, 2005: El Niño and greenhouse warming: Results from ensemble simulations with the NCAR CCSM. *J. Climate*, **18**, 4669–4683.

Copyright of Journal of Climate is the property of American Meteorological Society and its content may not be copied or emailed to multiple sites or posted to a listserv without the copyright holder's express written permission. However, users may print, download, or email articles for individual use.